Theory and experimental verification of a resultant response-based method for assessing the critical seismic excitation direction of curved bridges

Ruiwei Feng[1], Tongfa Deng[2,3], Tianpeng Lao[1], Anastasios G. Sextos[4], Wancheng Yuan[1*]

ABSTRACT

Previous studies have shown that the seismic incidence angle imposes a non-negligible impact on the seismic performance of curved bridges. The computational efficiency of some current methods for determining the critical angle needs to be improved and their applicability in practical engineering projects remains to be examined. For this reason, a resultant response-based (RRB) method is developed herein for assessing the critical excitation direction of curved bridges. To validate the feasibility of this method in an actual seismic design context, a 1/62.5-scale model of a three-span curved bridge is designed and a multi-angle shaking table test is implemented. Meanwhile, the finite-element model of the test specimen is set up, and the RRB method as well as the linear response-history analysis (LRHA) are comparatively assessed. The results indicate that the RRB method can

[1] State Key Laboratory of Disaster Reduction in Civil Engineering, Tongji University, Shanghai, China
[2] Jiangxi Provincial Key Laboratory of Environmental Geotechnical Engineering and Disaster Control, Jiangxi University of Science and Technology, Ganzhou, China.
[3] School of Architectural and Surveying & Mapping Engineering, Jiangxi University of Science and Technology, Ganzhou, China.
[4] Department of Civil Engineering, University of Bristol, Bristol, UK.
*Corresponding author
E-mail address: yuan@tongji.edu.cn (Wancheng Yuan)

capture the critical excitation direction of curved bridges with sufficient precision (error does not exceed 10% compared to LRHA). The associated computational effort is also substantially reduced given that RRB requires analysis solely along two orthogonal directions as the incidence angles, compared to standard response history analyses where ground motion excitation is applied at multiple ground motion orientations. The above observation is further verified by a well-designed experimental campaign, which demonstrates the accuracy and practicability of the RRB method for the case of realistic bridge configurations.

Keywords: Curved bridges, critical excitation directions, resultant response, shaking table, response spectrum

1. INTRODUCTION

By virtue of superior adaptability in densely populated areas and complex terrains, horizontally curved bridges have become common in urban overpasses and inter-city highways, hence, a considerable number of curved bridges are used as the lifeline system hubs to meet transport demands. Therefore, it is significant to guarantee the safety and functionality of curved bridges in their service period. Experience of the last fifty years, however, shows that curved bridges can be particularly vulnerable to seismic events [1–4]. In light of this issue, research efforts have been devoted to the study of seismic performance of curved bridges based on both deterministic [5–9] and probabilistic assessment [10–17].

The above studies mainly focused on the impact of bridge configuration, ground motion frequency content and numerical simulation methods. The direction of seismic excitation, which also has a major effect on their structural seismic responses [18–26], is only rarely considered. One of the reasons is that the angle of seismic incidence is random and not predictable, while its effect is more profound to curved bridges given their irregularity in plan and their distinct features in

terms of stiffness, strength, dynamic properties and damping [27–30]. Along these lines, it is important to ensure the reliability of seismic design of curved bridges, accounting for the peak responses of interest and the associated critical direction of excitation. The most common and direct method to predict the critical excitation direction is to implement a response history analysis (RHA) at multiple ground motion orientations and then compare the maximum response corresponding to each incidence angle (hereafter called direct analysis procedure [31]). The challenge here is that this method is computationally expensive and time consuming particularly for complex structures. Although provisions and specifications [32–34] recommend the use of a combination rule to estimate the peak seismic demand, which is a relatively simple way compared to the direct analysis procedure, it is still highly probable that seismic response is underestimated by the code provisions [35]. Given that the limitation of aforementioned methods, a number of methods aiming to directly determine the critical excitation direction of structures have been developed. The latter involve response spectrum analysis (RSA) [36], random vibration theory [37], linear response-history analysis (LRHA) [38], nonlinear static (i.e., pushover) analysis [39], nonlinear response history (NLRHA) and probabilistic fragility assessment [40] as well as lateral force analysis [41]. It is shown that the abovementioned methods enable a straightforward determination of the critical excitation direction of structures and are validated through other numerical approaches. On the other hand, there are still several issues that need to be improved. For instance, some of the existing methods predict the response components along a certain structural reference axis as the judging criterion for the critical excitation direction, which may not involve the responding contribution along the other orthogonal structural axis. Hence, the seismic performance of the whole structural member may

62 be misleading. Moreover, the critical angles for response quantities along different structural axes
63 can also vary, therefore, it is difficult to find a single critical angle for each structural member.
64 This is especially true for the case of curved bridges where, due to their geometric irregularity,
65 directions of principal axes (tangential and radial) for the various members are different, thus the
66 critical excitation direction of the major members may be very complex to predict. Additionally,
67 the majority of previous works are limited to analytical and numerical approaches, for simpler
68 structural systems and without experimental verification.

69 To test and verify the numerical results obtained from the theoretical derivation in a more
70 practical way, experimental investigation is essential. In recent years, shake table tests for bridge
71 structures were gradually carried out, including tests for the crucial bridge members (i.e. piers
72 [42–44], bearings [45], foundations [46]) as well as entire bridge structures [47–52].
73 Notwithstanding the progress made, the above tests study straight bridges with only few of them
74 focusing on curved ones. One example is the work of Williams and Godden [53] who conducted
75 a shake table study for the linear and nonlinear dynamic behavior of curved bridges and
76 emphasized the importance of seismic design in expansion joints. Yan et al. [54] evaluated the
77 efficiency of sliding isolation bearings in curved bridges while Li et al. [55] performed an
78 experimental study to assess the impact of ground motion spatial variability on the seismic
79 responses of curved bridges. Results showed that the curvature radius increases the sensitivity of
80 the bridge to the ground motion spatial variations, a result that can be mainly attributed to the
81 excitation of higher modes [56,57]. Zhang et al. [58] compared experimental and numerical
82 results of seismic damage for a small radius curved bridge considering the soil-structure
83 interaction (SSI) and reported that applying the equivalent soil springs method to simulate SSI

84 in the numerical model can gain approximate results to the actual ones. The aforementioned
85 experimental studies reveal that seismic performance of curved bridges is particularly complex
86 and highlight the effects of geometric parameters, seismic propagation process, and soil condition.
87 However, the impact of seismic excitation direction has not been yet taken into account.

88 Given the aforementioned issues and limitations in the development of theoretical methods
89 and the lack of experimental studies for the determination of critical excitation direction of
90 curved bridges, the peak resultant response quantity of interest, which is able to comprehensively
91 reflect the seismic behavior of the entire structural member, is proposed in this study as the key
92 proxy for identifying the critical excitation direction. Based on this evaluation measure, a
93 computationally efficient method, hereafter called "resultant response-based (RRB) method" is
94 presented for the determination of critical excitation direction of structures which is based on the
95 fundamentals of dynamics of structures and the RSA method. Subsequently, a 1/62.5-scaled
96 model of a three-span curved bridge is constructed and experimentally tested as a means to verify
97 the applicability of the RRB method. Results are also compared with numerical predictions using
98 standard LRHA to demonstrate the accuracy of this method.

99

100 # 2. DESCRIPTION OF THE RESULTANT RESPONSE-BASED METHOD

101 ## 2.1 Assumptions

102 In general, during dynamic analysis of structures, seismic excitation is applied along a pair of
103 orthogonal horizontal and one vertical orientations [59]. Particularly for multi-angle seismic analysis
104 however, Lopez and Torres [60] have shown that the critical excitation direction does not depend

105 on the vertical spectrum. Recently, Roy et al. [61] proposed the definition of the "most preferred"
106 angle of excitation, where the difference between bi-directional and uni-directional response is
107 minimized. In their study, they found that the structural peak response under unidirectional
108 excitation may considerably change with the incidence angle. Based on the foregoing observations,
109 they developed the relationship between the ratio of energetic length scale (L_e) of ground motion
110 components and the ratio of structural peak responses under bi-directional and unidirectional
111 excitation, respectively, thereby corroborating the existence of the most preferred angle which
112 corresponds to the neighborhood of the orientation where ratio of component L_e is maximized.
113 Based on their conclusions, one needs to identify the maximum response and the corresponding
114 seismic incidence angle by means of one-component ground motion, as an efficient prediction of the
115 peak response under bi-directional shaking so that the computational cost is greatly reduced. This
116 has motivated the authors to develop the RRB method based on the uni-directional seismic analysis.
117 The main steps of the methodology are outlined below.

118 Figure 1 illustrates the condition of a linear multi-degree-of-freedom (MDOF) structure or structural
119 member subjected to a horizontal time-variant seismic action $a(t)$. X and Y are the orthogonal
120 horizontal axes in the global coordinate system, while x and y are the local principal axes of the
121 member analyzed. Define θ as the reference angle from the X-axis to the direction of seismic
122 excitation $a(t)$ and let α represent the orientation of the resultant engineering demand
123 parameter R (e.g., displacement, stress, forces, etc.) with respect to the x-axis. Angles θ and α
124 are considered positive when they are measured counterclockwise. Seismic input excitation is
125 assumed to be a wide-band stationary process.

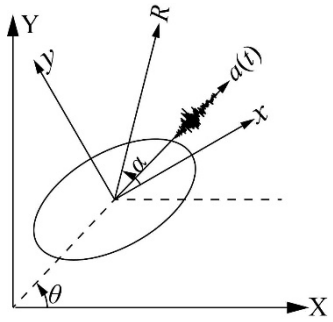

Figure 1: A linear structure or member under an arbitrarily unidirectional excitation

2.2 Fundamentals of the method

For a multi-degree-of-freedom, viscously damped, linear structure and based on the principle of modal superposition [62], the nodal displacement responses $\mathbf{u}(t)$ of the system can be written as:

$$\boldsymbol{u}(t) = \sum_{i=1}^{N} \Phi_i \eta_i(t) \quad (1)$$

where Φ_i is the ith modal vector, $\eta_i(t)$ is the modal coordinate for mode i and N is the number of modes analyzed. Thereby, the response quantities of interest, $R(t)$, are a linear combination of the nodal displacements $\mathbf{u}(t)$ and can be written as:

$$\mathrm{R}(t) = \mathbf{q}^{\mathrm{T}}\mathbf{u}(t) = \mathbf{q}^{\mathrm{T}}\sum_{i=1}^{N} \Phi_i \eta_i(t) \quad (2)$$

where $\mathbf{q}^{\mathrm{T}}$ is the transpose for the response transfer vector that are associated with structural geometry and stiffness properties.

Let S_a be the acceleration response spectrum for the seismic input $a(t)$. When the excitation is acting along the X-axis, according to the RSA method and derive the peak response quantities of interest along the x and y direction for mode i, respectively, $\overline{R_{i\mathrm{X}}^{x}}$ and $\overline{R_{i\mathrm{X}}^{y}}$ as:

$$\overline{R_{i\mathrm{X}}^{x}} = \mathbf{q}_{\mathrm{x}}^{\mathrm{T}} \boldsymbol{\Phi}_i \overline{\eta_{i\mathrm{X}}} \tag{3}$$

$$\overline{R_{i\mathrm{X}}^{y}} = \mathbf{q}_{\mathrm{y}}^{\mathrm{T}} \boldsymbol{\Phi}_i \overline{\eta_{i\mathrm{X}}} \tag{4}$$

140 in which

$$\overline{\eta_{i\mathrm{X}}} = \frac{S_i \Gamma_{i\mathrm{X}}}{\omega_i^2} \tag{5}$$

141 where $\mathbf{q}_x^{\mathrm{T}}$ and $\mathbf{q}_y^{\mathrm{T}}$ are the transposes for response transfer vectors for response quantities along
142 the x and y direction, respectively; $\overline{\eta_{i\mathrm{X}}}$ is the maximum modal coordinate for mode *i* when
143 acting the excitation along X-axis; S_i is the spectral value of the acceleration response spectrum for
144 the mode *i*; $\Gamma_{i\mathrm{X}}$ is the modal participation coefficient for mode *i* along X-axis and ω_i is the
145 circular frequency for mode *i*.

146 Consequently, the peak resultant response $\overline{R_{i\mathrm{X}}}$ for mode *i*, can be expressed as:

$$\overline{R_{i\mathrm{X}}} = \overline{R_{i\mathrm{X}}^{x}} \cos\alpha + \overline{R_{i\mathrm{X}}^{y}} \sin\alpha \tag{6}$$

147 Likewise, for the case of applying S_a along the Y-axis, the peak response quantities along the x
148 and y directions for mode *i*, respectively, $\overline{R_{i\mathrm{Y}}^{x}}$ and $\overline{R_{i\mathrm{Y}}^{y}}$ can be given as:

$$\overline{R_{i\mathrm{Y}}^{x}} = \mathbf{q}_{\mathrm{x}}^{\mathrm{T}} \boldsymbol{\Phi}_i \overline{\eta_{i\mathrm{Y}}} \tag{7}$$

$$\overline{R_{i\mathrm{Y}}^{y}} = \mathbf{q}_{\mathrm{y}}^{\mathrm{T}} \boldsymbol{\Phi}_i \overline{\eta_{i\mathrm{Y}}} \tag{8}$$

149 in particular

$$\overline{\eta_{iY}} = \frac{S_i \Gamma_{iY}}{\omega_i^2} \quad (9)$$

150 where $\overline{\eta_{iY}}$ is the maximum modal coordinate for mode i under the excitation along direction Y
151 and Γ_{iY} is the modal participation coefficient for mode i along the Y-axis. Thereby, the peak
152 resultant response for mode i, $\overline{R_{iY}}$, can be expressed as:

$$\overline{R_{iY}} = \overline{R_{iY}^{x}} \cos\alpha + \overline{R_{iY}^{y}} \sin\alpha \quad (10)$$

153 When S_a acts along an arbitrary angle of incidence θ, the resultant response quantity of interest
154 for mode i, $\overline{R_{i\theta}}$, can be determined as:

$$\overline{R_{i\theta}} = \overline{R_{iX}} \cos\theta + \overline{R_{iY}} \sin\theta \quad (11)$$

155 It should be noted that the algebraic sum in equation (11) is due to the fact that the ground motion
156 component $(a(t)\cos\theta)$ along X-axis and $(a(t)\sin\theta)$ along Y-axis are completely correlated.
157 Substituting the equation (6) and equation (10) into equation (11) gives:

$$\begin{aligned} \overline{R_{i\theta}} = &(\overline{R_{iX}^{x}} \cos\alpha + \overline{R_{iX}^{y}} \sin\alpha)\cos\theta \\ &+ (\overline{R_{iY}^{x}} \cos\alpha + \overline{R_{iY}^{y}} \sin\alpha)\sin\theta \end{aligned} \quad (12)$$

158 Combining equation (3) and equation (4) as well as equation (7) and equation (8), equation (12) can
159 be rewritten as:

$$\begin{aligned} \overline{R_{i\theta}} = &(\boldsymbol{q}_{\mathrm{x}}^{\mathrm{T}} \Phi_i \cos\alpha + \boldsymbol{q}_{\mathrm{y}}^{\mathrm{T}} \Phi_i \sin\alpha)\overline{\eta_{i\mathrm{X}}}\cos\theta \\ &+ (\mathbf{q}_{\mathrm{x}}^{\mathrm{T}} \Phi_i \cos\alpha + \mathbf{q}_{\mathrm{y}}^{\mathrm{T}} \Phi_i \sin\alpha)\overline{\eta_{i\mathrm{Y}}}\sin\theta \end{aligned} \quad (13)$$

160 Note that the peak modal coordinates, $\overline{\eta_{iX}}$ and $\overline{\eta_{iY}}$ appear simultaneously and the ratio

161 $\overline{\eta_{iX}} / \overline{\eta_{iY}}$ is a constant, which can be verified using equation (5) divided by equation (9) as:

$$\overline{\eta_{iX}} / \overline{\eta_{iY}} = \frac{\Gamma_{iX}}{\Gamma_{iY}} \tag{14}$$

162 Therefore, the peak resultant response quantity of interest for a structure subjected to the seismic
163 excitation in an arbitrary direction θ, $\overline{R_\theta}$, can be obtained using the Complete Quadratic
164 Combination (CQC) method [63] as:

$$\overline{R_\theta} = \sqrt{\sum_{i=1}^{N}\sum_{j=1}^{N} \rho_{ij}\, \overline{R_{i\theta}}\,\overline{R_{j\theta}}} \tag{15}$$

165 where the correlation coefficient between responses in mode i and j, ρ_{ij}, is also taken from the [63].

166 Substituting equation (13) into equation (15) leads to:

$$\overline{R_\theta} = \sqrt{\sum_{i=1}^{N}\sum_{j=1}^{N} \rho_{ij} (\cos^2\theta D_1 + \sin^2\theta D_2 + 2\sin\theta\cos\theta D_3)} \tag{16}$$

167 In particular,

$$D_1 = \overline{R_{iX}^x R_{jX}^x}\cos^2\alpha + 2\overline{R_{iX}^x R_{jX}^y}\cos\alpha\sin\alpha + \overline{R_{iX}^y R_{jX}^y}\sin^2\alpha \tag{17a}$$

$$D_2 = \overline{R_{iY}^x R_{jY}^x}\cos^2\alpha + 2\overline{R_{iY}^x R_{jY}^y}\cos\alpha\sin\alpha + \overline{R_{iY}^y R_{jY}^y}\sin^2\alpha \tag{17b}$$

$$D_3 = \overline{R_{iX}^x R_{jY}^x}\cos^2\alpha + \overline{R_{iX}^y R_{jY}^y}\sin^2\alpha + \overline{R_{iX}^x R_{jY}^y}\cos\alpha\sin\alpha + \overline{R_{iY}^x R_{jX}^y}\cos\alpha\sin\alpha \tag{17c}$$

168 On the basis of equation (16), the critical excitation direction for the structure, θ_{cr}, can be obtained
169 by means of computer programming by following the three steps outlined below:

(i) Apply spectrum S_a along the direction X and analyze the structure to calculate the peak modal responses $\overline{R_{i\mathrm{X}}^{x}}$, $\overline{R_{i\mathrm{X}}^{y}}$ given by Equations (3) and (4),

(ii) Apply spectrum S_a along the direction Y and analyze the structure to calculate the modal responses $\overline{R_{i\mathrm{Y}}^{x}}$, $\overline{R_{i\mathrm{Y}}^{y}}$ from Equations (7) and (8),

(iii) By means of computer programming and for a given incidence angle $\theta_{i(i=1,2,\ldots n)}$, loop the responding direction $\alpha_{i(i=1,2,\ldots n)}$ over 360° with a specified interval (e.g. 3°) to calculate the peak responses with respect to the incidence angle θ_i, $\overline{R_{\theta_i}}$, determined by Equations (15)-(17) and then compare the peak responses with various incidence angles to determine the critical excitation direction θ_{cr}.

It can be seen from the derivation process of RRB method that the critical excitation direction (θ_{cr}) with regard to the overall seismic response of a structural component can be obtained meanwhile the computational costs are significantly reduced by using computer programming with the aid of only two angles of seismic incidence compared to the standard response history analyses along multiple angles of seismic incidence.

3. BRIDGE MODEL DESIGN AND INSTRUMENTATION

To verify the validity of the RRB method, a typical horizontally curved, continuous, reinforced concrete (RC) bridge was selected as the prototype bridge for experimental verification. Figure 2 shows the geometric configuration of this bridge with a length of 75 m, three equal spans and a radius (R) of 50 m measured to the centerline of the deck. The deck consists of a single-cell box girder section with 8.5 m width and 1.9 m depth which is supported by four single-pier bents. For each bent, the pier is composed of solid circular RC sections with a height of 10 m and a diameter of 1.9 m. Two

laminated rubber bearings are set on each cap beam to connect the superstructure with the substructure. Moreover, the deck, cap beams and piers are constructed using the Chinese Grade C40 concrete [64].

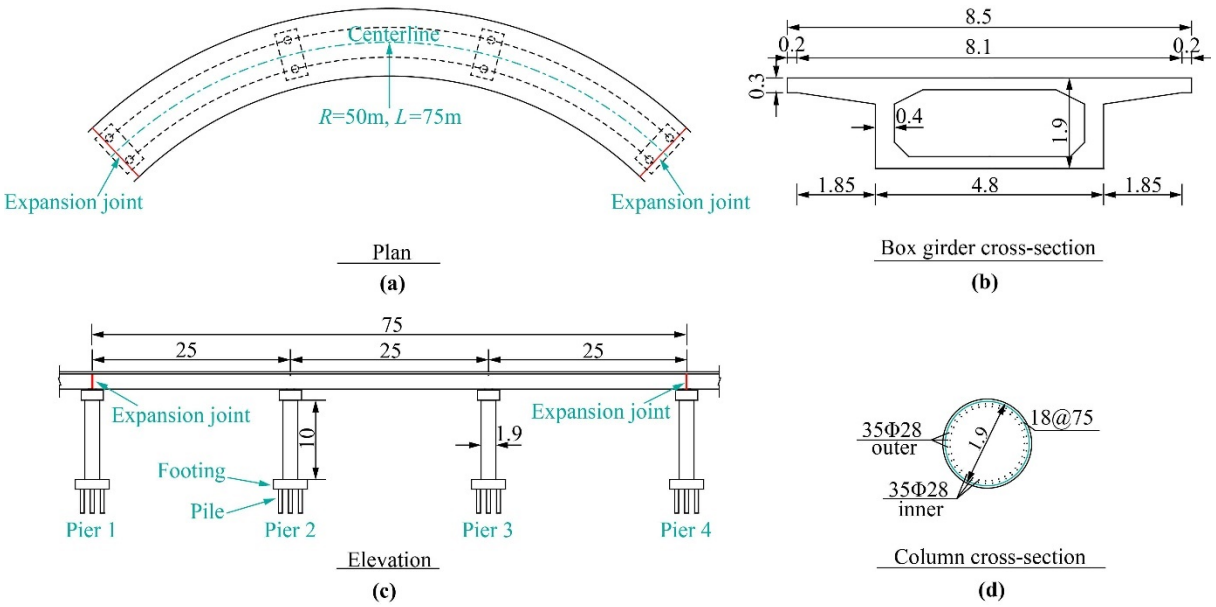

Figure 2: Configuration of the prototype (units: m): (a) plan, (b) box girder cross-section, (c) elevation, (d) pier cross-section.

3.1 Similitude Requirements

Determination of the scale factor is key in experimental model design. Generally, the elastic modulus (E), acceleration (a) and length (l) are selected as three fundamental physical quantities considering the simplicity and convenience for controlling them at the early stage of the test. Based on dimensional analysis and combined with equation of motion, similitude requirements for dynamic models can be written as [65]:

$$\frac{S_E}{S_\rho S_a S_l} = 1 \tag{18}$$

where S_E, S_ρ, S_a, S_l are scale factors of elastic modulus, material density, acceleration and length, respectively.

Given the limitation of the shaking table dimensions, the test model was geometrically scaled to 1/62.5 ($S_l = 1/62.5$) of the prototype bridge. Besides, as the RRB method is based on the RSA method, which is applicable to linear structural systems only, a material with equivalent elastic properties was selected. In particular, polymethylmethacrylate (PMMA) was selected for the deck and bents of the scaled model. Assuming the elastic modulus of 2600Mpa for PMMA [66], the scale factor (S_E) for the elastic modulus can be calculated equal to 0.08. Moreover, to obtain a reasonable mass for the bridge model, the mass scale factor, which depends on the three key fundamental quantities, should be also determined. In light of the fixed value for S_E / S_l, considering the limited actuation and load capacity of the shaking table, the acceleration scale factor (S_a) was set equal to 3, which is within the reasonable value range suggested in the literature [66].

Table 1: Similitude requirements of the curved bridge model

Physical quantity	Dimension	Similitude relation	Scale factor
Length, *l*	**[L]**	**S_l**	**0.016**
Acceleration, *a*	**[LT^{-2}]**	**S_a**	**3**
Elastic modulus, *E*	**[FL^{-2}]**	**S_E**	**0.08**
Displacement, δ	[L]	$S_\delta = S_l$	0.016
Strain, ε	/	$S_\varepsilon = 1$	1
Stress, σ	[FL^{-2}]	$S_\sigma = S_E$	0.08
Equivalent mass density, ρ	[FL^{-4}T^2]	$S_\rho = S_E/(S_l S_a)$	1.667
Mass, m	[FL^{-1}T^2]	$S_m = S_E S_l^2 / S_a$	0.00000683
Area, S	[L^2]	$S_S = S_l^2$	0.000256
Stiffness, k	[FL^{-1}]	$S_k = S_E S_L$	0.00128
Time, t	[T]	$S_t = (S_l/S_a)^{0.5}$	0.073
Moment, M	[FL]	$S_M = S_E S_l^3$	0.000000328
Force, F	[F]	$S_F = S_E S_l^2$	0.00002048
Velocity, v	[LT^{-1}]	$S_v = (S_a S_l)^{0.5}$	0.219

Note: [F] = Force; [L]= Length; [T]=Time

Based on the known fundamental scale factors, the other scale factors required in the bridge model design can be calculated through the similitude relations given in Table 1, with the results also listed in the same table.

3.2 Design of the scaled model

Having listed the similitude requirements in Table 1, the dimensions of the scaled model were decided. Figure 3 presents the geometric configuration of the scaled model.

To facilitate the selection of the PMMA sheet specification and reduce the assembly difficulty of the model, as shown in Figure 3(a), the girder adopted the rectangular hollow cross-section. Given that the axial stiffness is not a dominant factor for the seismic response of the bridge model, the cross-section of the girder was designed to match the scale factor of flexural and torsional stiffness. To ensure an elastic model, the material of the bearing still employed rubber, and the upper and lower surfaces of the bearing were fixed with the girder and cap beam, respectively. The bearing had a circular cross-section, with both its diameter and height taken equal to 10 mm based on the stiffness scale factor. Considering that the bearing has small dimensions and can experience multiple seismic cycles during testing and to reduce the chances of accidental bearing failure during the experimental campaign, a simple replacement device for the bearing was invented as illustrated in Figure 3(b). It can be seen that the bearings can be replaced by removing the bolts connecting the inner and outer flange plates.

Regarding the substructure, the bridge has four single-pier bents (Figure 2). Solid circular cross-sections were adopted for the piers of the scaled model and were fixed on a rigid base. As the loading is applied unidirectionally by the shaking table, the base is designed to be rotatable in order to achieve the multi-angle excitation. For this purpose, two arc-shaped slots were designed for the base. The positions of the slots depend on the hole sites of the countertop, which means that there should be enough holes so that the base and the countertop can be bolted together firmly. The geometric details

241 and the working principle for the rotatable base are displayed in Figure 3(c) and Figure 3(d),
242 respectively.

243 Additionally, to meet the similitude requirements for the dynamic characteristics, additional artificial
244 masses were attached to the scaled model. As shown in Figure 3(e), for the superstructure, a total of
245 5.02 kg additional masses was uniformly distributed along the deck, while for the substructure, 0.95
246 kg lumped additional masses were placed on the cap beam for each bent. Figure 4 presents a schematic
247 view of the curved bridge model.

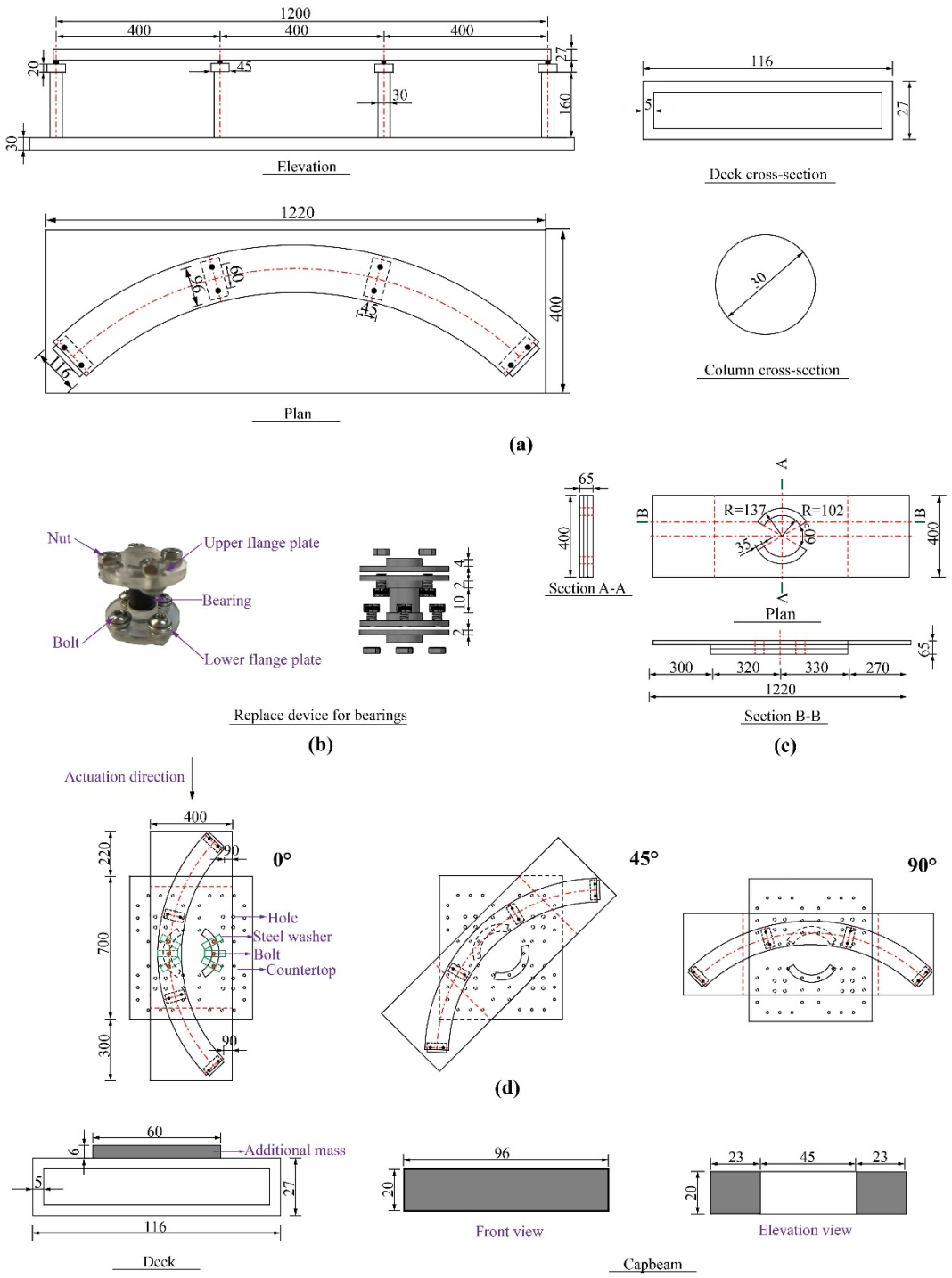

Figure 3: Geometric configuration of the scaled model (units: mm): (a) geometric dimensions of the scaled model, (b) bearing replacement device, (c) geometric dimensions of the rotatable base, (d) working principle of the rotatable base, (e) additional mass arrangement.

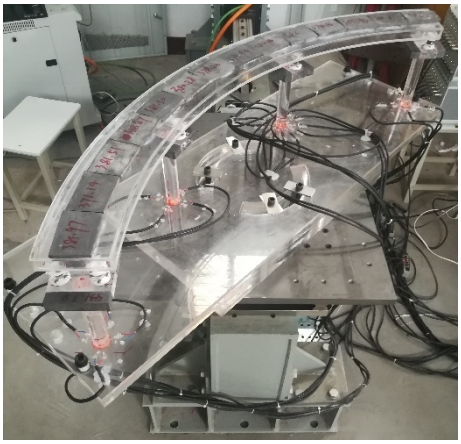

Figure 4: Schematic view of the curved bridge model

3.3 Mechanical property tests of model members

In the process of determining the similitude requirements for the scaled model, theoretical mechanical properties for the model members were utilized. However, due to discrepancies in specimen specification, test environment and processing techniques, the actual mechanical properties for the members are different from the theoretical ones. Therefore, to gain accurate numerical results so as to make comparison with the experimental data, mechanical property tests for major model members are necessitated. Previous studies [67] have shown that the dynamic modulus of elasticity (E_d) of a polymer may not be equal to its static modulus, hence, a test for the dynamic elastic modulus of PMMA members was implemented as shown in Figure 5. One end of the test specimen was fixed through the clamp, while the other end hung the weight using the rope; then rope was cut and the specimen started free vibration; meanwhile, the strain attenuation curves of the specimen were recorded and the fundamental period could be determined. According to the undamped free vibration equation of distributed-parameter system [62], the fundamental circular frequency, ω_1 , is given by:

$$\omega_1 = 1.875^2 \sqrt{\frac{E_d I}{\overline{m} L^4}} \quad (19)$$

where I is the flexural moment of inertia of the specimen; $\overline{m}$ is the mass per unit length and L is the span of the distributed-parameter system.

The dynamic elastic modulus of the specimen can be obtained based on equation (19) as:

$$E_d = \frac{\omega_1^2 \overline{m} L^4}{12.360 I} \quad (20)$$

Another consequence of the small size of the rubber bearings for the scaled model, is that conventional quasi-static experimental setups are not applicable to test their shear stiffness. For this reason, a simple device for approximately testing the shear stiffness was designed. Figure 6 presents the device structure and the test method. The upper and lower surfaces of the bearings were glued with the cover plates, respectively. The upper cover plate was connected with the weights through the wire rope and the lower plate was fixed on the table. When the weights were applied, the bearings produced shear deformations which were recorded by the dial gauge. Thereby, the approximate shear stiffness of the bearing, k_b, was derived as:

$$k_b = \frac{m_w g}{n \overline{\delta}} \quad (21)$$

where m_w is the mass of the weight; n is the number of tested bearings and $\overline{\delta}$ is the average displacement of the left and right dial gauges.

By gradually increasing the weight mass, the shear stiffness of the bearing tended to be constant and was adopted as the shear stiffness for the bearing. Figure 7 shows the test results for the shear stiffness

of the bearings and Table 2 summarizes the mechanical properties of the structural members.

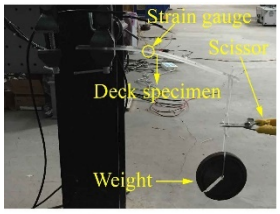

Deck specimen

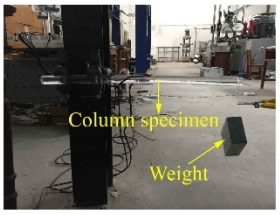

Column specimen

Figure 5: Test method for the dynamic elastic modulus of the members

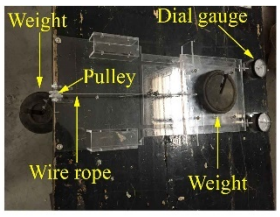

Test device

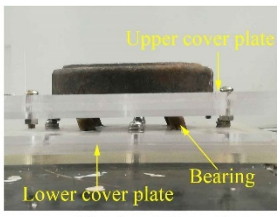

Bearing deformation

Figure 6: Test method for the shear stiffness of the bearings

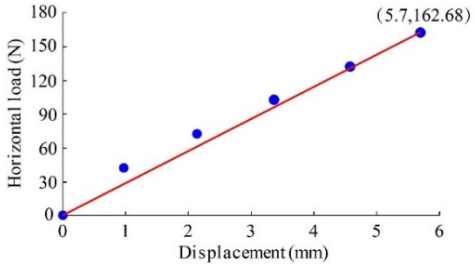

Figure 7: Test results for the shear stiffness of the bearings

Table 2: Mechanical properties of the members for the scale model

Member	Shear stiffness (kN/m)	Dynamic elastic modulus (GPa)
Bearing	7.126	—
Deck	—	1.620
Pier	—	3.095

3.4 Instrumentation

To capture the response quantities of interest under seismic excitation, the scaled model was instrumented with 26 transducers, including 8 displacement markers, 2 accelerometers and 16 strain gages. Figure 8 shows the instrumentation details of the scaled model. Unlike straight bridges, nodal displacements of the curved bridge are not just along the excitation direction. Accordingly, the NDI Optotrak Certus optical measurement system (resolution of displacement: 0.01 mm) produced by Northern Digital Inc. was employed to track the three-dimensional nodal displacements of the scaled model. Five displacement markers were arranged along the deck, two were placed on the cap beam of the side bents, and one was set in the middle of the base as the reference point for the measurement.

The two accelerometers were installed orthogonally in the middle of the deck to monitor the accelerations along the tangential and radial directions with respect to the midpoint of the deck. Additionally, four strain gages (electrical resistance = 120 Ω ± 0.1%, gauge factor = 2.08 ± 1% and measuring range = 1×10^{-6} ε-15000 ε) were pairwise orthogonally attached on each pier to measure the average section curvatures in the local directions. All the measurement data was monitored by a multifunctional data-acquisition system produced by Jiangsu Donghua Testing Technology Co. Ltd with a sampling rate of 500 Hz.

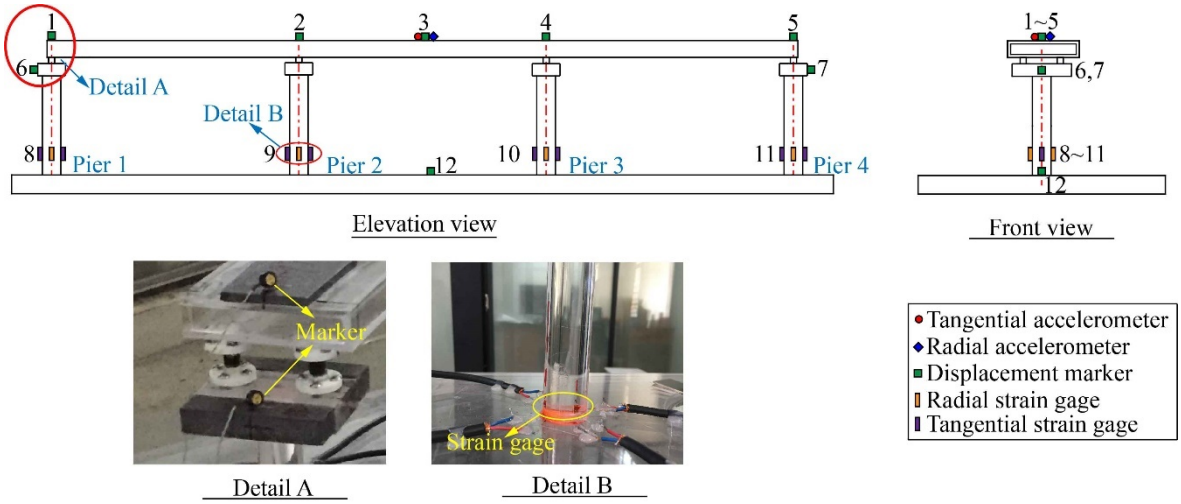

Figure 8: Instrumentation details of the scaled model

4. EXPERIMENTAL PROGRAM

The scaled model was tested at the Civil and Mechanical Experimental Center in Jiangxi University of Science and Technology. Figure 9 shows the details of the shake table system, mainly including a 0.6 m × 0.7 m countertop and a unidirectional actuator with a working frequency of 200 Hz. The payload of the shake table system was 100 kilos for an acceleration of 1.5g.

4.1 Input ground motion

A typical far-field ground motion record was selected as the seismic input, namely, one component

of the 1992 Landers earthquake ground motion (station: LA-116th St School, identifier: RSN865_LANDERS_116000). Because of the 1/62.5 geometric scale and 3/1 acceleration scale, the time coordinate of the input ground motion was compressed by a factor of 13.693. Besides, considering the large stiffness of the scaled model and in order to excite discernible responses and ensure measurement accuracy, the selected ground motion record was amplified up to 1g. The input motion with a compressed time axis and the corresponding response spectrum with 5% damping ratio are shown in Figures 10(a) and 10(b), respectively. In order to examine the earthquake simulation of the shake table testing system, input signal was compared with the output achieved motions as shown in Figure 11. Meanwhile, as the excitation shall be implemented multiple times considering the effect of ground motion directionality, the achieved acceleration-time records by the shake table for different seismic incidence angles (eg., 0°, 45° and 90°) were compared and plotted in Figure 12. As a result, a good agreement is presented among the achieved motions. Hence, the achieved acceleration-record was adopted as the excitation for the numerical analyses to eliminate the effect caused by the error between the original input signal and the output motions.

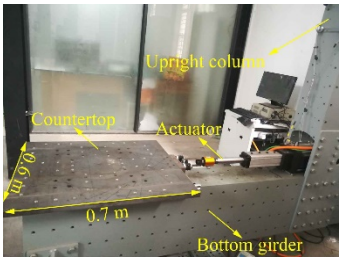

Figure 9: Details of the shaking table system

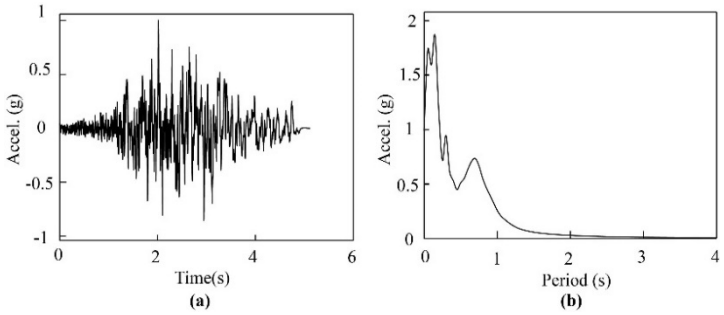

Figure 10: Input ground motion: (a) acceleration time history and (b) acceleration response spectrum with 5% damping

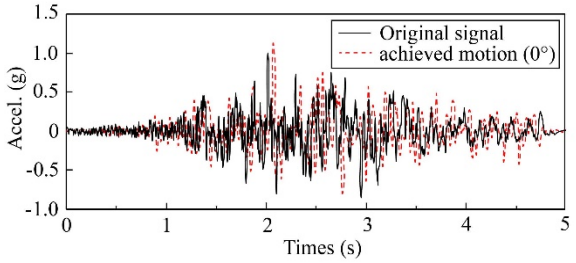

Figure 11: Comparison between the original signal and the achieved motion by the shake table

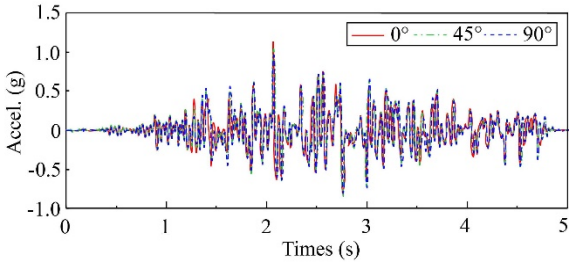

Figure 12: Comparison of achieved motions and for the cases of different excitation directions

4.2 Test cases

Table 3 lists the test case arrangements for the scaled model. To evaluate the applicability and efficiency of the RRB method, the scaled model should be shaken by omnidirectional seismic actions (from 0° to 360°). As the curved bridge model is symmetric with respect to the transversal axis (global Y-axis), the angle of seismic incidence is only needed to vary from 0° to 180°. Therefore, in this test, the scaled model was rotated clockwise for the interval $0^{\circ} \le \theta \le 180^{\circ}$ at incremental angles of 15°. White-noise excitations were also applied throughout the test to help identify the modal properties of the scaled model.

Table 3: Shake table test cases for the curved bridge model

Case name	Input motion	PGA(g)	Input direction
W-0	White noise	0.3g	0°
L-0	Landers	1g	0°
L-15	Landers	1g	15°
L-30	Landers	1g	30°
L-45	Landers	1g	45°
L-60	Landers	1g	60°
L-75	Landers	1g	75°
W-90	White noise	0.3g	90°
L-90	Landers	1g	90°
L-105	Landers	1g	105°
L-120	Landers	1g	120°
L-135	Landers	1g	135°
L-150	Landers	1g	150°
L-165	Landers	1g	165°
L-180	Landers	1g	180°

5. NUMERICAL APPLICATION AND EXPERIMENTAL VERIFICATION

Based on the fundamentals mentioned in section 2.2, the RRB method was applied to the numerical model of the curved bridge specimen. Then the numerical results were compared with the test results to evaluate the applicability and efficiency of the RRB method.

5.1 Finite-element model

The finite-element (FE) model of the curved bridge test specimen was developed using the commercially available software SAP2000 [68]. Figure 13 illustrates the FE model of the 1/62.5-scaled bridge. The deck and bents were simulated adopting the elastic beam-column elements, while the cross-sectional properties for the members were determined based on the geometric configuration in Figure 2. The Young's modulus of the deck and piers employed the measured data presented in Table 2, namely, 1.620 GPa and 3.095 GPa. The rubber bearing was simulated using the linear link with the tested horizontal shear stiffness of 7.126 kN/m. Soil-structure interaction was not able to be captured in the shake table test, therefore all the bents were assumed fixed at their bottoms. A damping ratio of 5% was adopted for all modes. Natural vibration periods and frequencies of the scaled model are illustrated in Table 4. Figure 14 shows that the fundamental vibration mode is the radial mode of the deck, while the second and third are predominantly tangential and torsional modes of the deck, respectively.

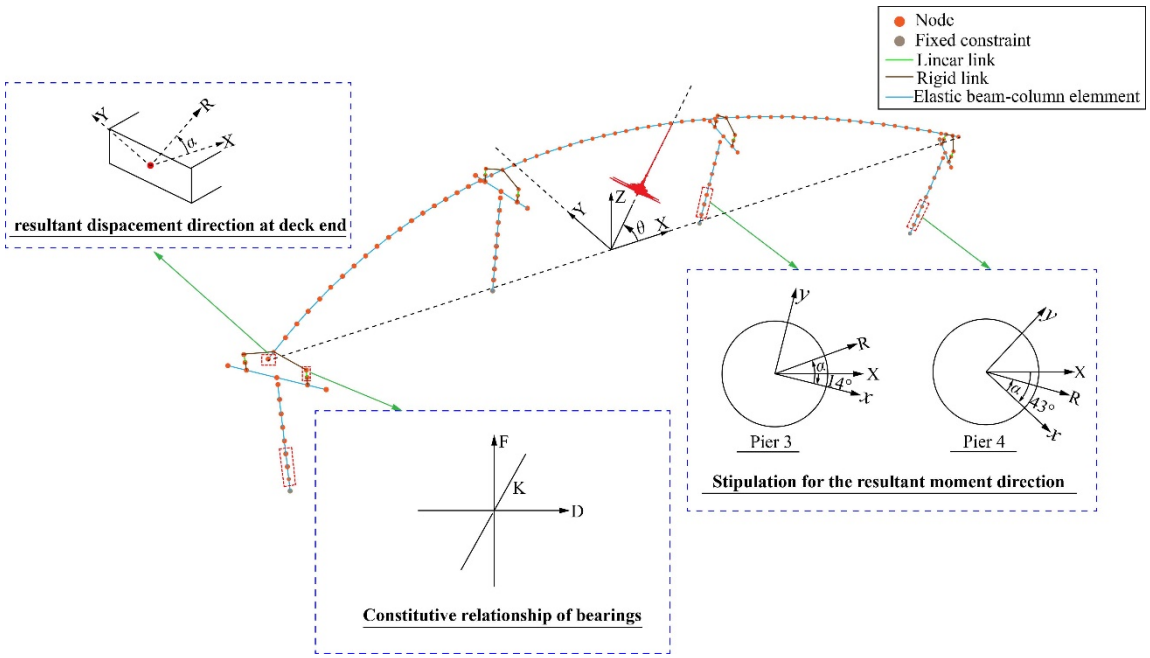

Figure 13: Numerical model of the test curved bridge

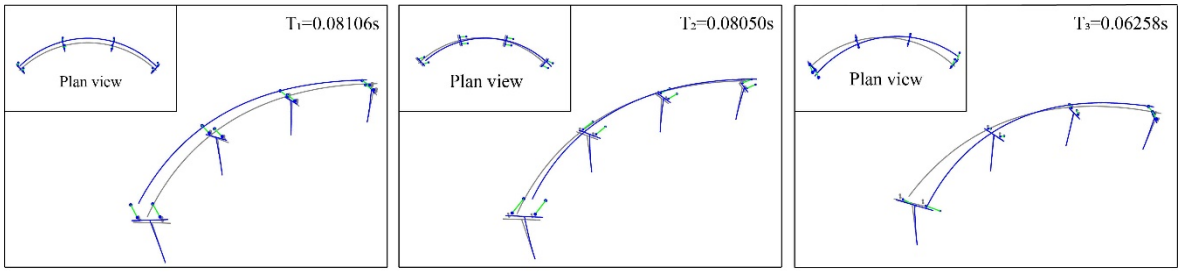

Figure 14: First three mode shapes of the scaled model: (a) first mode, (b) second mode, (c) third mode

Table 4: Natural vibration periods and frequencies of the scaled model

Mode	Period (s)	Frequency (Hz)
1	0.081	12.337
2	0.081	12.422
3	0.063	15.979
4	0.021	46.958
5	0.021	47.214
6	0.021	47.314

7	0.021	47.622
8	0.021	47.752
9	0.019	53.260
10	0.019	53.894
11	0.018	55.000
12	0.016	63.145

368

369 As already mentioned for the testing protocol, the actual motion achieved by the shake table was
370 applied to the numerical model and rotated by multiple angles. Figure 13 illustrates the angle of
371 seismic incidence θ with respect to the included angle between the input motion and axis X. To be
372 consistent with the shake table test, the angle θ was varied from 0° to 180° with increments of 15°
373 and θ increasing in the counterclockwise direction.
374 As a consequence of the geometric symmetry of the scaled model, the resultant moments at the
375 bottom of Pier 3 and Pier 4, and the resultant deck-end displacement close to the Pier 1 (hereafter
376 called deck displacement) were selected to represent the structural response. The stipulation for the
377 direction of resultant response, α, is also shown in Figure 13. For the piers, α refers to the resultant
378 direction relative to the x-axis which corresponds to the tangential direction of the piers, while in
379 terms of the deck displacement, α denotes the angle between the resultant responding direction
380 and the X-axis. Note that angle α is taken to be positive counterclockwise.

381 **5.2 Finite-element model validation for bridge model**

382 To verify the accuracy of the design for the scaled model, the dynamic characteristics and the response

383 histories of the test model were compared with the FE model. As shown in Figure 15, the fundamental
384 frequency of the scaled model is 12.512 Hz and the corresponding vibration mode is the radial one,
385 which is quite close to the fundamental frequency of the numerical model (12.337 Hz). The minor
386 error (1.42%) is deemed satisfactory as per the scaled model design.
387 To identify the agreement between the seismic performance of experiment and the numerical model
388 under the multi-angle excitations, response histories of deck displacement and moment of Pier 3 were
389 compared for different incidence angles, 15° and 135°, as presented in Figures 16 and Figure 17. Table
390 5 compares the measured and numerically identified peak responses of the scaled model. It can be
391 seen that the peak responses of both the experimental and the numerical model are reasonably close,
392 with an average error of 26.7% for the deck displacement and 14.4% for the pier moment, respectively.
393 Compared to the case of pier moment, the larger error for the deck displacement comparison is
394 because the round marker has a small glued contact area with deck (Figure 8, detail A) and could
395 slightly vibrate with respect to the girder during the shake table test, therefore the displacement
396 information obtained from the reflected signal of the marker was affected considering the actual small
397 deck displacement itself, thereby a certain additional error for the displacement measurement is
398 introduced compared to that of the pier moment. Although the experimental results are generally
399 more fluctuant, it can be seen from Figure 16 and 17 that the phase changes of the seismic response
400 identified experimentally are relatively in line with the numerical model, which indicates that the
401 peak responses of the numerical model can be approximately captured by the test when subjected to
402 multidirectional seismic excitations. As a result, it can be used to efficiently evaluate the applicability
403 of the RRB method.

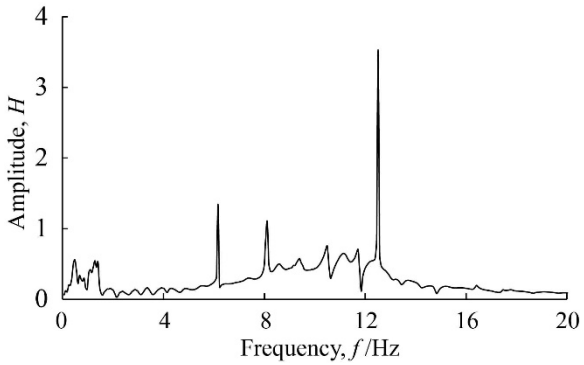

Figure 15: Fourier spectra of transverse acceleration response on the top of the deck

Table 5: Comparison of the peak responses between test model and numerical model

Incidence angle	Deck displacement (mm)				Moment of Pier 3 (N·m)			
	X direction		Y direction		*x* direction		*y* direction	
	Measured results	Numerical results	Measured results	Numerical results	Measured results	Numerical results	Measured results	Numerical results
15°	3.23	2.82 (-14.6%)	2.79	2.00 (-39.5%)	5.20	7.25 (+28.3%)	2.39	2.88 (+16.9%)
135°	2.33	1.97 (-18.2%)	2.34	1.74 (-34.5%)	6.48	7.28 (+11.0%)	4.68	4.62 (+1.31%)

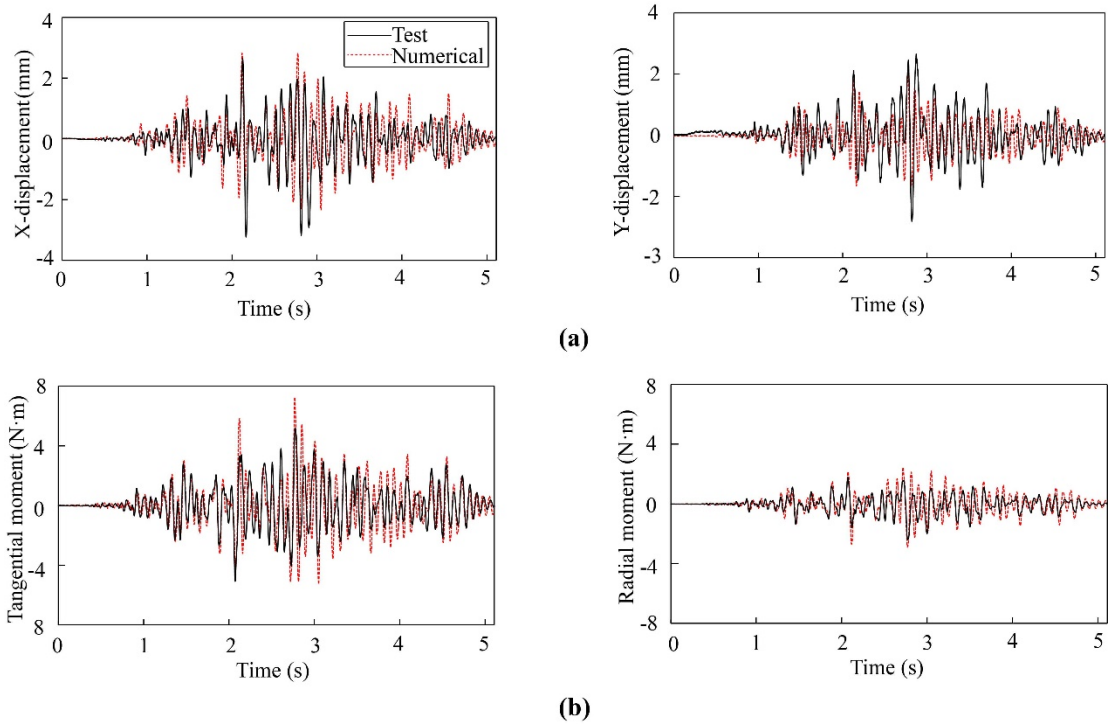

Figure 16: Comparison of seismic response time histories with respect to θ=15°: (a) deck displacement and (b) moment of Pier 3

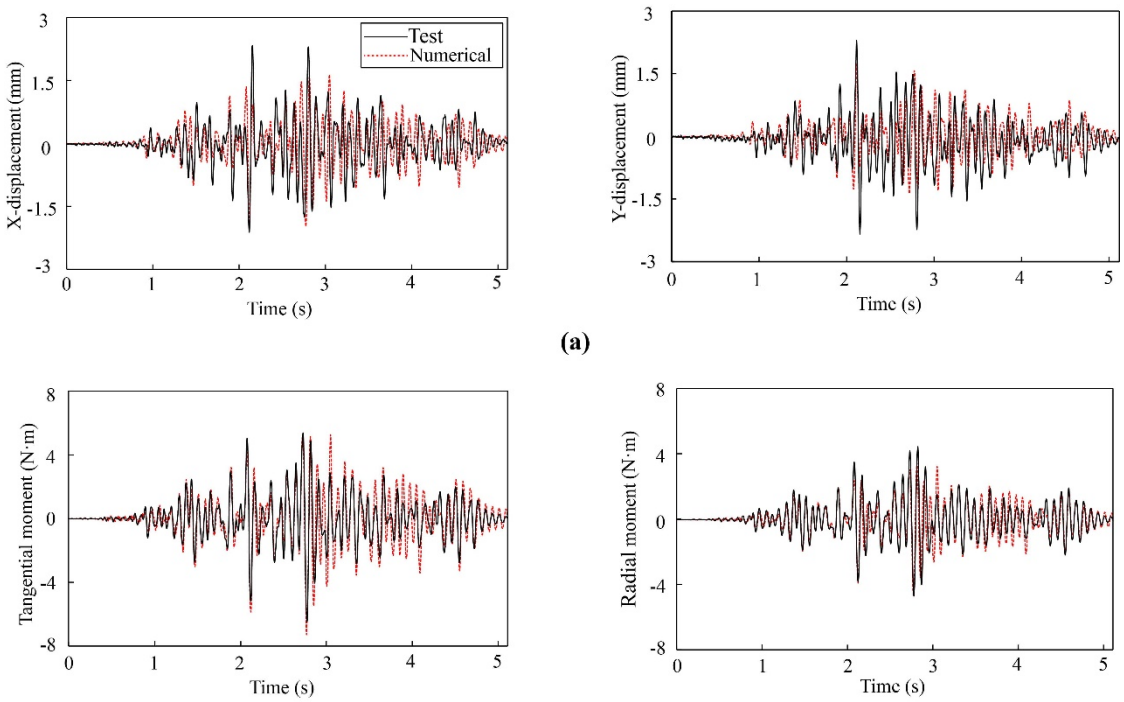

Figure 17: Comparison of seismic response time histories with respect to θ=135°: (a) deck displacement and (b) moment of Pier 3

5.3 Comparison of numerical and experimental results

As described earlier, RRB method is able to predict the variation of peak resultant pier moments and deck displacements with respect to the incidence angle. See step (i) and step (ii) as described in Section 2.2, the peak modal responses along the local axes for the pier moment and deck displacement were derived and were displayed in Tables 6 and 7, respectively. Using the results in Table 6 and Table 7, the relationship between the peak response and the excitation direction can be established from step (iii).

To verify the theoretical reliability and practical applicability of the RRB method, the peak resultant responses under multi-directional excitations were also calculated using the LRHA and test data, that is, responses in two orthogonal directions were combined by the Square-Root-of-Sum-of-Squares (SRSS) rule [69] through the entire history of excitation and the maximum was taken as the peak

one. Figure 18 compares the peak resultant responses predicted by the RRB method with those derived by means of LRHA and the shake table test.

Table 6: Peak modal responses for the pier moment along local axes

Mode	Moment of Pier 3 (N · m)				Moment of Pier 4 (N · m)			
	$R_{i\mathrm{X}}^{x}$	$R_{i\mathrm{X}}^{y}$	$R_{i\mathrm{Y}}^{x}$	$R_{i\mathrm{Y}}^{y}$	$R_{i\mathrm{X}}^{x}$	$R_{i\mathrm{X}}^{y}$	$R_{i\mathrm{Y}}^{x}$	$R_{i\mathrm{Y}}^{y}$
1	-0.410	-0.090	-7.210	-1.580	-0.330	-0.270	-5.750	-4.830
2	-0.460	7.540	0.030	-0.410	-1.750	6.870	0.110	-0.400
3	-0.720	0.090	-0.020	0.000	-1.840	-0.840	-0.040	-0.010
4	0.040	-0.070	0.210	-0.370	0.060	-0.040	0.320	-0.190
5	-0.010	-0.070	-0.020	-0.070	-0.020	0.060	-0.020	0.050
6	0.010	-0.200	0.010	0.010	-0.020	0.210	0.010	0.000
7	-0.050	-0.090	0.480	0.900	-0.070	-0.120	0.810	1.310
8	0.070	-1.150	0.010	-0.070	0.100	-1.340	-0.010	0.060
9	0.010	-0.010	0.360	-0.050	0.010	-0.010	0.020	0.040
10	0.340	0.030	0.020	0.000	0.800	0.040	0.050	0.000
11	-0.020	-0.010	0.170	0.020	-0.010	-0.010	0.040	-0.010
12	0.010	0.010	0.100	0.010	-0.010	0.000	-0.100	0.000

Table 7: Peak modal responses for the bearing displacement

Mode	Deck displacement (mm)			
	$R_{i\mathrm{X}}^{x}$	$R_{i\mathrm{X}}^{y}$	$R_{i\mathrm{Y}}^{x}$	$R_{i\mathrm{Y}}^{y}$
1	0.016	0.195	0.286	3.438
2	2.856	1.029	-0.174	-0.063
3	0.372	-0.923	0.007	-0.017
4	0.002	-0.002	0.013	-0.013
5	0.000	0.000	0.000	0.000
6	0.000	0.000	0.000	0.000
7	-0.003	0.003	0.031	-0.028
8	0.009	0.010	0.001	0.001
9	0.001	-0.001	-0.032	0.039
10	0.002	-0.006	0.000	0.000
11	0.000	0.000	-0.001	0.002
12	0.000	0.000	0.002	-0.002

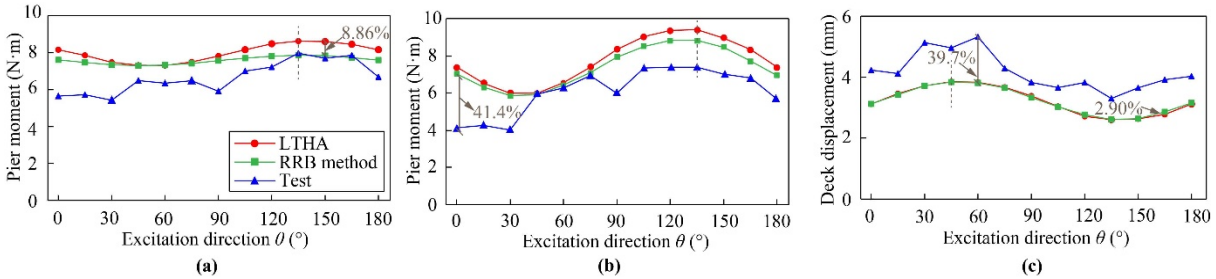

Figure 18: Variation of the peak resultant responses with regard to the excitation direction based on the RRB method, LRHA, and the shaking table test: (a) Pier 3, (b) Pier 4, (c) deck displacement

It can be seen that the variations of peak resultant responses with respect to the excitation direction are in good agreement for the three methods. The critical excitation direction for the pier moment is 135°, while for the deck displacement is 45°. This indicates that applying the ground motion component only along the principal bridge axes (tangential and radial directions with respect to the middle point of the bridge) as it is commonly prescribed by the codes, may underestimate the seismic response of curved bridges at least when the resultant response is used as the evaluation criterion. The results derived from the RRB method match well with those of LRHA with the maximum difference of 8.86% and 2.90% for the pier moment and deck displacement, respectively. This verifies that the RRB method is able to identify the critical excitation direction with acceptable errors and without significant computational cost. Moreover, for the same bridge member, the maximum discrepancies of the peak responses amongst various incidence angles are 36.4% and 32.3% for Pier 4 and deck displacement, and 15.1% for Pier 3. This is evidence that at least for the curved bridge studied, seismic responses of the piers close to the deck-end are more sensitive to the excitation direction than those near the mid-span.

On the other hand, the experimental results demonstrate that the scaled model remains elastic, which satisfies the prerequisite of the RRB method. Specifically, the moment of Pier 3 at θ = 135° as the

critical response among piers (as shown in Figure 18) was selected to examine the state of piers and bearings. As the Pier 3 is simultaneously subjected to the vertical axial force (F_v) and the flexural moment (M), the conditions for the pier to remain elastic are expressed as:

$$\left|\frac{M}{W}\right| + \left|\frac{F_v}{A}\right| \leq [\sigma_c] \quad (22a)$$

$$\left|\frac{M}{W}\right| - \left|\frac{F_v}{A}\right| \leq [\sigma_t] \quad (22b)$$

where A is the gross area of the pier section, W is the section modulus of the pier, and $[\sigma_c]$ and $[\sigma_t]$ are the permissible compression and tensile stress of the PMMA, respectively. In this study, F_v equals to 20 N (including partial masses of the deck, masses of cap beam and pier as well as the additional artificial masses applied on the deck and cap beam), M is 7.975 N· m, A is 7×10^{-4} m^2 and W is 2.65×10^{-6} m^3. According to the previous studies [70], $[\sigma_c]$ and $[\sigma_t]$ are more than 100 MPa under the dynamic strain-rate ($\geq 10^3$ s^{-1} [71]) loading condition such as seismic loading. Substituting the specific geometric and mechanical parameters into Eqs. (22a) and (22b) and they are satisfied as:

$$\left|\frac{M}{W}\right| + \left|\frac{F_v}{A}\right| = 3.04 \text{ MPa} \leq [\sigma_c] \ (> 100 \text{ MPa}) \quad (23a)$$

$$\left|\frac{M}{W}\right| - \left|\frac{F_v}{A}\right| = 2.98 \text{ MPa} \leq [\sigma_t] \ (> 100 \text{ MPa}) \quad (23b)$$

Based on the above results, the actual tensile and compression stresses do not exceed the permissible threshold values, which effectively means the piers remains elastic during the test. For bearings, it can be seen from the Figure 7 that the bearing is approximately linearly elastic when the horizontal load

is less than 162.68 N. On the basis of the moment of Pier 3, the shear force (F_s) of the bearing can be calculated as:

$$F_s = \frac{M}{L} \tag{24}$$

where L is the height from the pier bottom to the middle of the bearing and equals to 0.185 m. Substituting the specific values of M and L into Eq. (24), the shear force of the bearing can be obtained as:

$$F_s = \frac{M}{L} = \frac{7.975}{0.185} = 43.12\ \text{N} < 162.68\ \text{N} \tag{25}$$

Hence, the bearing also remains within the elastic regime. Along these lines, the entire scaled model was validated in the elastic domain during the test. Based on the aforementioned verifications, the applicability of the RRB method for the case of a realistic bridge configuration is highlighted by contrast with the experimental results. As shown in Figure 18, the variation of peak resultant responses that develop at the deck and piers as well as the critical angle captured by the RRB method are approximately consistent with those identified by the experiment. The peak values of piers experimentally observed are smaller than those predicted by the RRB method with the maximum error of 41.4%, while the peak deck displacements tested are larger compared to those obtained from the RRB method with the maximum error of 39.7%. There are four reasons for the discrepancies observed between the numerical and experimental results:

(a) Given that the dimensions of the rubber bearings with a diameter and height of 10 mm, their shear stiffness can only be approximately measured by the simple device invented and shown in Figure 6. This naturally introduces a certain error in terms of equivalent stiffness. Based on the

observation in Figure 18, it is indicated that the actual stiffness of the bearing could be smaller than the measured ones taken from the test.

(b) The accumulated error when combining the measured response components by means of the SRSS rule could affect the prediction of the actual resultant responses.

(c) As stated in Section 5.2, the slight vibration of the marker with respect to the deck during the test could introduce a certain error to the acquisition of the real deck displacement.

(d) Considering the payload of the shaking table, the PMMA which has small density is selected as the material for the small-scale model in this study. Because the mechanical properties of the PMMA are sensitive to the temperature and loading mode [72], there is a degree of uncertainty that is introduced. In case of a large-scale test, steel would be a better option given its stable mechanical properties.

Despite of the aforementioned source of discrepancies from the particular test, as displayed in Figure 18, the test and numerical results show the same trend in terms of the peak resultant responses. As a result, it can be concluded that this test confirms the validity of the RRB method and as such, the conclusions drawn are valid for a full-scale (i.e., real) bridge as well. Besides, it can be found from Figure 18(c) that the that the critical excitation direction of the deck displacement for the numerical results is $\theta = 45°$ while the test shows a different critical incidence angle ($\theta = 60°$), followed closely by $\theta = 30°$. This observation is because the peak deck displacements obtained from the numerical results (e.g., RRB method) for $\theta = 30°, 45°$ and $60°$ are 3.72 mm, 3.84 mm and 3.81 mm, respectively, which are very close with each other. Therefore, the test does not actually clearly identify the critical excitation direction.

Taking the case of Pier 3 as an example, Figure 19 illustrates the variation of the moment component with respect to the excitation direction. It is evident that the numerical and experimental variation of the bending moment component with the incidence angle is in better agreement compared to the case where the composition of response components is plotted, which verifies the effect of accumulated error produced when combining the response components measured by means of the SRSS rule. On the other hand, Figure 19 also corroborates that the critical incidence angle for different response components varies: θ=165° is the critical direction for the moment along x-axis, while the peak moment along y-axis appears for an excitation angle of θ=75°. By contrast, considering the resultant moment as the evaluation criterion, the RRB method is able to catch the unique critical excitation direction for the pier (θ=135° as mentioned in this section). Hence, it can be seen that the RRB method can not only comprehensively reflect the seismic performance of the entire structural member but also be more convenient to be carried out in the practical seismic design of the structure.

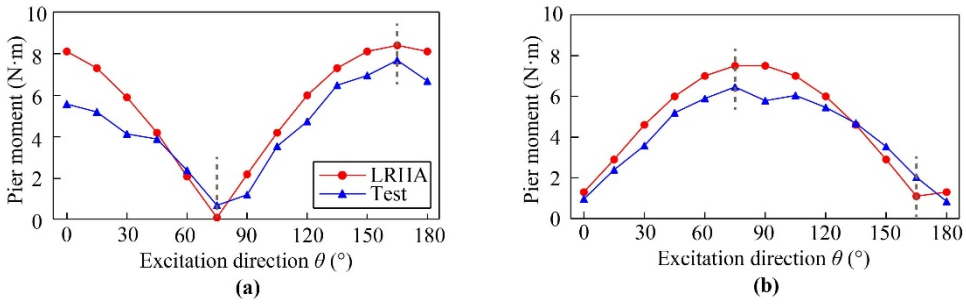

Figure 19: Variation of the moment component of the Pier 3 with respect to the excitation direction (numerical prediction and shake table test measured response): (a) direction x and (b) direction y

6. CONCLUSIONS

An analytical, response resultant-based (RRB) method is developed in this paper for assessing the critical excitation direction of curved bridges. The specific formulae were derived based on the fundamentals of structural dynamics and RSA method to capture the critical angle and demand. In

535 order to evaluate the efficiency and applicability of the RRB method for the case of a realistic curved
536 bridge configuration, a shaking table study of a 1/62.5-scale three-span curved bridge model was
537 conducted for several excitation directions. Then, the RRB method as well as the LRHA were also
538 comparatively assessed. The main conclusions and findings are summarized as follows:

539 1. Considering the resultant response quantity of interest as the evaluation criterion of the critical
540 excitation direction is a pragmatic approach that is able to comprehensively reflect the seismic
541 performance of the entire structural member and associate it with a unique critical incidence
542 angle. This approach is not only computationally efficient in comparison with taking the
543 individual response components along the local axes but is also more meaningful in terms of
544 structural design.

545 2. The RRB method proposed herein was found able to assess the critical excitation direction of the
546 curved bridge example with sufficient precision (deviation did not exceed 10% compared to the
547 results of LRHA) while the computational efforts were drastically reduced (the ground motion
548 was only applied twice) by means of computer programming.

549 3. For the horizontally curved bridge studied, and assuming the resultant response as the judging
550 criterion for critical angle of incidence, the application of input motion along the principal bridge
551 axes only (i.e., tangential and radial directions with respect to the middle point of the bridge) may
552 underestimate the actual response and thereby lead to unconservative seismic design. Bridge bent
553 piers that are close to the deck-end show higher sensitivity to the excitation direction compared
554 to those located near the mid-span.

555 4. The results of multi-angle shaking table test are capable to capture the variation of peak resultant

response as a function of the excitation direction. They also verify the applicability and efficiency of the RRB method for the case of a realistic curved bridge. However, the differences between actual mechanical properties of the members and their measure ones, the accumulated error caused by the combination of the tested orthogonal response components using the SRSS rule and the slight vibration of the marker itself with respect to the deck during the test, cause a non-negligible deviation from the theoretically and numerically expected response.

5. The RRB method is a useful alternative to standard multi-angle response history analysis and is appropriate for the prediction of the critical excitation direction of a curved bridge responding elastically. However, further research is needed given that the critical angle is different for different structural components and for each engineering demand parameter. It is also important to extend the relevant research to the nonlinear field.

CREDIT AUTHORSHIP CONTRIBUTION STATEMENT

Ruiwei Feng: Methodology, Software, Validation, Formal analysis, Investigation, Data Curation, Writing - Original Draft, Writing - Review & Editing, Visualization. **Tongfa Deng:** Investigation, Resources, Funding acquisition. **Tianpeng Lao:** Methodology, Software, Validation, Investigation, Data Curation. **Anastasios Sextos:** Writing – Review & Editing, Supervision. **Wancheng Yuan:** Conceptualization, Methodology, Writing - Review & Editing, Supervision, Project administration, Funding acquisition.

ACKNOWLEDGEMENT

This research was supported by the National Natural Science Foundation of China under Grant No. 51778471, 51978512; the Ministry of Science and Technology of China under Grant No. SLDRCE19-B-19; and Science and Technology Project of Communications Department of Jiangxi Province under Grant No. 2016C0006. The first author also thanks for the financial support from the China Scholarship Council (CSC). Special thanks to Mr. Weibin Li, Mr. Rihao Mai and Mr. Yi Wang for

their generous assistances and valuable suggestions during the experiment. The authors would also acknowledge the anonymous reviewers who have contributed to improving and enriching the paper.

REFERENCES

[1] Tseng WS, Penzien J. Seismic response of long multiple-span highway bridges. Earthq Eng Struct Dyn 1975;4:25–48. doi:10.1002/eqe.4290040103.

[2] Buckle IG. The Northridge, California earthquake of January 17, 1994: Performance of highway bridges. Report no. NCEER-94-0008. Buffalo, New York; 1994.

[3] Han Q, Du X, Liu J, Li Z, Li L, Zhao J. Seismic damage of highway bridges during the 2008 Wenchuan earthquake. Earthq Eng Eng Vib 2009;8:263–73. doi:10.1007/s11803-009-8162-0.

[4] Kawashima K, Takahashi Y, Ge H, Wu Z, Zhang J. Reconnaissance Report on Damage of Bridges in 2008 Wenchuan, China, Earthquake. J Earthq Eng 2009;13:965–96. doi:10.1080/13632460902859169.

[5] Jennings PC, Housner GW, Hudson DE, Trifunac MD, Frazier GA, Wood JH et al, editor. Engineering features of the San Fernando earthquake of February 9, 1971. Report no EERI. 71-02. California Institute of Technology, Pasadena; 1971.

[6] Abdel-salam MN, Heins CP. Seismic response of curved steel box girder bridges. J Struct Eng 1989;114(12):2790–800.

[7] Mwafy A, Elnashai A, Yen W-H. Implications of Design Assumptions on Capacity Estimates and Demand Predictions of Multispan Curved Bridges. J Bridg Eng 2007; 12(6):710–26.

[8] Wu H, Najjar WS. Parametric seismic analysis of curved steel box-girder bridges with two continuous spans. Bridg Struct 2007;3 (3-4): 205–13. doi:10.1080/15732480701511989.

[9] Falamarz-Sheikhabadi MR, Zerva A. Analytical seismic assessment of a tall long-span curved reinforced-concrete bridge, Part I: numerical modeling and input excitation. J Earthq Eng 2017;21:1305–34. doi:10.1080/13632469.2016.1211565.

[10] Seo J, Linzell DG. Horizontally curved steel bridge seismic vulnerability assessment. Eng Struct 2012;34:21–32. doi:10.1016/j.engstruct.2011.09.008.

[11] Seo J, Linzell DG. Use of response surface metamodels to generate system level fragilities for existing curved steel bridges. Eng Struct 2013;52:642–53. doi:10.1016/j.engstruct.2013.03.023.

[12] AmiriHormozaki E, Pekcan I. Analytical fragility functions for horizontally curved steel I-girder highway bridges. Earthq Spectra 2014.

[13] Pahlavan H, Zakeri B, Amiri GG, Shaianfar M. Probabilistic vulnerability assessment of horizontally curved multiframe RC box-girder highway bridges. J Perform Constr Facil 2015;30 (3):4015038. doi:10.1061/(ASCE)CF.1943-5509.0000780.

[14] Jeon J-S, DesRoches R, Kim T, Choi E. Geometric parameters affecting seismic fragilities of curved multi-frame concrete box-girder bridges with integral abutments. Eng Struct 2016;122:121–43. doi:10.1016/j.engstruct.2016.04.037.

[15] Sarraf Shirazi R, Pekcan G, Itani A. Analytical fragility curves for a class of horizontally curved box-girder bridges. J Earthq Eng 2018;22(5):881–901. doi:10.1080/13632469.2016.1264325.

[16] Abbasi M, Abedini MJ, Zakeri B, Ghodrati Amiri G. Seismic vulnerability assessment of a Californian multi-frame curved concrete box girder viaduct using fragility curves. Struct Infrastruct Eng 2016;12(12):1585–601. doi:10.1080/15732479.2016.1152586.

[17] Rogers LP, Seo J. Vulnerability sensitivity of curved precast-concrete I-girder bridges with various configurations subjected to multiple ground motions. J Bridg Eng 2017;22(2):04016118. doi:10.1061/(ASCE)BE.1943-5592.0000973.

[18] Rigato A, Medina RA. Influence of angle of incidence on seismic demands for inelastic single-storey structures subjected to bi-directional ground motions. Eng Struct 2007;29:2593–601. doi:10.1016/j.engstruct.2007.01.008.

[19] Torbol M, Shinozuka M. Effect of the angle of seismic incidence on the fragility curves of bridges. Earthq Eng Struct Dyn 2012. doi:10.1002/eqe.2197

[20] Kalkan E, Reyes JC. Significance of rotating ground motions on behavior of symmetric- and asymmetric-plan structures: Part I. Single-story structures. Earthq Spectra 2015;31(3):1591–612. doi:10.1193/072012EQS241M.

[21] Huang JQ, Du XL, Jin L, Zhao M. Impact of incidence angles of P waves on the dynamic responses of long lined tunnels. Earthq Eng Struct Dyn 2016;45(15):2435–54. doi:10.1002/eqe.2772.

[22] Jeon J, Choi E, Noh M-H. Fragility characteristics of skewed concrete bridges accounting for ground motion directionality. Struct Eng Mech 2017; 63(5):647–57. doi:10.12989/sem.2017.63.5.647.

[23] Vargas Alzate YF, Pujades Beneit LG, Barbat AH, Hurtado Gomez JE, Diaz Alvarado SA. Probabilistic seismic damage assessment of reinforced concrete buildings considering directionality effects. Struct Infrastruct Eng 2018;14(6):817–29. doi:10.1080/15732479.2017.1385089.

[24] Song J, Gao Y, Feng T. Probabilistic assessment of earthquake-induced landslide hazard including the effects of ground motion directionality. Soil Dyn Earthq Eng 2018;105:83–102. doi:10.1016/j.soildyn.2017.11.027.

[25] Moschonas IF, Kappos AJ. Assessment of concrete bridges subjected to ground motion with an arbitrary angle of incidence: static and dynamic approach. Bull Earthq Eng 2013;11(2):581–605. doi:10.1007/s10518-012-9395-2.

[26] Lagaros ND. Multicomponent incremental dynamic analysis considering variable incidence angle. Struct Infrastruct Eng 2010;6(1-2):77–94. doi:10.1080/15732470802663805.

[27] Araújo M, Marques M, Delgado R. Multidirectional pushover analysis for seismic assessment of irregular-in-plan bridges. Eng Struct 2014;79:375–89. doi:10.1016/j.engstruct.2014.08.032.

[28] Ni Y, Chen J, Teng H, Jiang H. Influence of earthquake input angle on seismic response of curved girder bridge. J Traffic Transp Eng (English Ed) 2015;2(4):233–41. doi:10.1016/j.jtte.2015.05.003.

[29] Sextos AG, Manolis, GD. Dynamic Response of Infrastructure to Environmentally Induced Loads. vol. 2. Cham: Springer International Publishing; 2017. doi:10.1007/978-3-319-56136-3.

[30] Feng R, Wang X, Yuan W, Yu J. Impact of seismic excitation direction on the fragility analysis of horizontally curved concrete bridges. Bull Earthq Eng 2018;16:4705–33. doi:10.1007/s10518-018-0400-2.

[31] Archila M, Ventura CE, Liam Finn WD. New insights on effects of directionality and duration of near-field ground motions on seismic response of tall buildings. Struct Des Tall Spec Build 2017;26:e1363. doi:10.1002/tal.1363.

[32] AASHTO. LRFD bridge design specification. American Association of State Highway and Transportation Officials, Washington, DC. 2012. doi:10.2337/dc12-1714.

[33] Caltrans SD. Caltrans seismic design criteria version 1.7. Sacramento, CA: California Department of Transportation; 2013.

[34] CEN. EN 1992-1-1. Eurocode 8: design of structures for earthquake resistance-part2: bridges. Brussels (Belgium): Comité Européen de Normalisation; 2005. doi:10.1680/cien.144.6.55.40618.

[35] Bisadi V, Head M. Evaluation of Combination Rules for orthogonal seismic demands in nonlinear time history analysis of bridges. J Bridg Eng 2011;16(6):711–7. doi:10.1061/(ASCE)BE.1943-5592.0000241.
[36] Wilson EL, Button MR. Three-dimensional dynamic analysis for multi-component earthquake spectra. Earthq Eng Struct Dyn 1982;10(3):471-6.
[37] Smeby W, Der Kiureghian A. Modal combination rules for multicomponent earthquake excitation. Earthq Eng Struct Dyn 1985;13(1):1–12. doi:10.1002/eqe.4290130103.
[38] Athanatopolou AM. Critical orientation of three correlated seismic components. Eng Struct 2005;27(2):301-312. doi:10.1016/j.engstruct.2004.10.011
[39] Song B, Pan JS, Liu Q. Study on critical angle to the seismic response of curved bridges based on pushover method. In: Proceedings of the 14th World Conference Earthquake Engineering. Beijing, China, 2008.
[40] Taskari O, Sextos AG. Multi-angle, multi-damage fragility curves for seismic assessment of bridges. Earthq Eng Struct Dyn 2015;44:2281–301. doi:10.1002/eqe.2584.
[41] Skoulidou D, Romão X. Critical orientation of earthquake loading for building performance assessment using lateral force analysis. Bull Earthq Eng 2017;15(12):5217–46. doi:10.1007/s10518-017-0176-9.
[42] Kawashima K, Zafra R, Sasaki T, Kajiwara K, Nakayama M. Effect of Polypropylene Fiber Reinforced Cement Composite and Steel Fiber Reinforced Concrete for Enhancing the Seismic Performance of Bridge Piers. J Earthq Eng 2011;15(8):1194–211. doi:10.1080/13632469.2011.569051.
[43] Kawashima K, Zafra RG, Sasaki T, Kajiwara K, Nakayama M, Unjoh S, Sakai J, Kosa K, Takahashi Y, Yabe M. Seismic performance of a full-size polypropylene fiber-reinforced cement composite bridge pier based on E-defense shake table experiments. J Earthq Eng 2012;16:463–95. doi:10.1080/13632469.2011.651558.
[44] Yuan W, Guo A, Yuan W, Li H. Shaking table tests of coastal bridge piers with different levels of corrosion damage caused by chloride penetration. Constr Build Mater 2018;173:160–71. doi:10.1016/j.conbuildmat.2018.04.048.
[45] Li H, Tian S, Dang X, Yuan W, Wei K. Performance of steel mesh reinforced elastomeric isolation bearing: Experimental study. Constr Build Mater 2016;121:60–8. doi:10.1016/j.conbuildmat.2016.05.143.
[46] Wang X, Shang Y, Ye A. Shaking table tests on seismic failure mechanism of elevated-pile- foundation-supported bridges in liquefied or nonliquefiable soil. In: Proceedings of the 16th World Conference Earthquake Engineering Santiago, Chile, 2017.
[47] Chen X, Guan Z, Li J, Spencer Jr BF. Shake table tests of tall-pier bridges to evaluate seismic performance. J Bridg Eng 2018;23(9):04018058. doi:10.1061/(ASCE)BE.1943-5592.0001264.
[48] Li J, Xiang N, Tang H, Guan Z. Shake-table tests and numerical simulation of an innovative isolation system for highway bridges. Soil Dyn Earthq Eng 2016;86:55–70. doi:10.1016/j.soildyn.2016.05.002.
[49] Shaban N, Caner A. Shake table tests of different seismic isolation systems on a large scale structure subjected to low to moderate earthquakes. J Traffic Transp Eng (English Ed.) 2018; 5(6): 480-490. doi: 10.1016/j.jtte.2018.10.003.
[50] Shaban N, Caner A, Yakut A, et al. Vehicle effects on seismic response of a simple-span bridge during shake tests. Earthq Eng Struct Dyn 2015, 44(6): 889-905. doi: 10.1002/eqe.2491.
[51] Yang H, Pang Y, Tian S, Dang X, Yuan W. Case study of the seismic response of an extra-dosed cable-stayed bridge with cable-sliding friction aseismic bearing using shake table tests. Struct Des Tall Spec

Build 2017;26:e1398. doi:10.1002/tal.1398.
[52] Li J, Yan J, Peng T, Han L. Shake table studies of seismic structural systems of a Taizhou Changjiang highway bridge model. J Bridg Eng 2014;20:04014065. doi:10.1061/(ASCE)BE.1943-5592.0000650.
[53] Williams D, Godden W. Seismic response of long curved bridge structures: Experimental model studies. Earthq Eng Struct Dyn 1979;7(2):107–28. doi:10.1002/eqe.4290070202.
[54] Yan L, Li Q, Han C, Jiang H. Shaking Table Tests of Curved Bridge considering Bearing Friction Sliding Isolation. Shock Vib 2016;4:1–14. doi:10.1155/2016/6245062.
[55] Li X, Zhang DY, Yan W, Chen YJ, Xie WC. Shake-Table Test for a Typical Curved Bridge : Wave Passage and Local Site Effects. J Bridg Eng 2014;20(2):04014061. doi:10.1061/(ASCE)BE.1943-5592.0000643.
[56] Sextos AG, Karakostas C, Lekidis V, Papadopoulos SP. Multiple support seismic excitation of the Evripos bridge based on free-field and on-structure recordings. Struct Infrastruct Eng 2015;11:1510–23. doi:10.1080/15732479.2014.977302.
[57] Papadopoulos SP, Sextos AG. Anti-symmetric mode excitation and seismic response of base-isolated bridges under asynchronous input motion. Soil Dyn Earthq Eng 2018;113:148–61. doi:10.1016/j.soildyn.2018.06.004.
[58] Zhi Z, Xiaojun L, Riqing L, Chenning S. Shaking table tests and numerical simulations of a small radius curved bridge considering SSI effect. Soil Dyn Earthq Eng 2019;118:1–18. doi:10.1016/j.soildyn.2018.12.006.
[59] Penzien J, Watabe M. Characteristics of 3-dimensional earthquake ground motions. Earthq Eng Struct Dyn 1975;3:365–73.
[60] López OA, Torres R. The critical angle of seismic incidence and the maximum structural response. Earthq Eng Struct Dyn 1997;26:881–94. doi:10.1002/(SICI)1096-9845(199709)26:9<881::AID-EQE674>3.0.CO;2-R.
[61] Roy A, Santra A, Roy R. Estimating seismic response under bi-directional shaking per uni-directional analysis: Identification of preferred angle of incidence. Soil Dyn Earthq Eng 2018;106:163–81. doi:10.1016/j.soildyn.2017.12.022.
[62] Chopra AK. Dynamics of structures: theory and applications to earthquake engineering. Upper Saddle River: NJ: Prentice Hall; 1995.
[63] Wilson EL, Der Kiugeghian A, Bayo EP. A replacement for the SRSS method in seismic analysis. Earthq Eng Struct Dyn 1981;9(4):187–92.
[64] Ministry of Transport of the People's Republic of China (MOT), 2004. JTG D62-2004 Specifications for design of highway reinforced concrete and prestressed concrete bridges and culverts. China Communications Press, Bejing [in Chinese].
[65] Krawinkler H, Moncarz PD. Similitude requirements for dynamic models. Special Publication 1982;73(1):1–22.
[66] Zhou Y, Lu XL. Method and technology for shaking table model test of building structures. Beijing: Science Press; 2016. [In Chinese].
[67] Pringle OA, Harker RJ. Environmental fatigue testing of molded plastics for prosthetic heart valves. Exp Mech 1969;9(4):171–8.
[68] Habibullah A, Wilson EL. SAP2000: integrated finite element analysis and design of structures. Comput Struct Inc,: Berkeley, California, 1997.
[69] Buckle I, Friedland I, Mander J, Martin G, Nutt R, Power M. Seismic retrofitting manual for highway structures: part 1 – bridges. Technical report, MCEER-06-SP10, Multidisciplinary Center for

751 Earthquake Engineering Research, StateUniversity of New York at Buffalo, NY, USA; 2006.
752 [70] Lee OS, Kim MS. Dynamic material property characterization by using split Hopkinson pressure bar
753 (SHPB) technique. Nucl Eng Des 2003; 226:119-125. doi: 10.1016/S0029-5493(03)00189-4.
754 [71] Blumenthal WR, Cady CM, Lopez, MF, et al. Influence of temperature and strain rate on the
755 compressive behavior of PMMA and polycarbonate polymers. AIP Conference Proceedings 2002;
756 620(1): 665-668. doi: 10.1063/1.1483626.
757 [72] Arruda EM, Boyce MC, Jayachandran R. Effects of strain rate, temperature and thermomechanical
758 coupling on the finite strain deformation of glassy polymers. Mech. Mater 1995; 19(2-3): 193-212. doi:
759 10.1016/0167-6636(94)00034-E

This is to conform that all authors named in the manuscript are aware of the submission and have agreed for the paper to be submitted to Engineering Structures.

Sincerely,

Wancheng Yuan

The authors' individual contributions to the paper are outlined below:

Ruiwei Feng: Methodology, Software, Validation, Formal analysis, Investigation, Data Curation, Writing - Original Draft, Writing - Review & Editing, Visualization. **Tongfa Deng:** Investigation, Resources, Funding acquisition. **Tianpeng Lao:** Methodology, Software, Validation, Investigation, Data Curation. **Anastasios Sextos:** Writing – Review & Editing, Supervision. **Wancheng Yuan:** Conceptualization, Methodology, Writing - Review & Editing, Supervision, Project administration, Funding acquisition.

Sincerely,

Wancheng Yuan